PNAS RESEARCH ARTICLE | PHYSICS OPEN ACCESS

Transport coefficient approach for characterizing nonequilibrium dynamics in soft matter

HongRui He[a,b], Heyi Liang[b], Miaoqi Chu[c], Zhang Jiang[c], Juan J. de Pablo[a,b,1], Matthew V. Tirrell[a,b,1], Suresh Narayanan[c,1], and Wei Chen[a,b,1]

Edited by David Weitz, Harvard University, Cambridge, MA; received January 18, 2024; accepted June 16, 2024

Nonequilibrium states in soft condensed matter require a systematic approach to characterize and model materials, enhancing predictability and applications. Among the tools, X-ray photon correlation spectroscopy (XPCS) provides exceptional temporal and spatial resolution to extract dynamic insight into the properties of the material. However, existing models might overlook intricate details. We introduce an approach for extracting the transport coefficient, denoted as $J(t)$, from the XPCS studies. This coefficient is a fundamental parameter in nonequilibrium statistical mechanics and is crucial for characterizing transport processes within a system. Our method unifies the Green–Kubo formulas associated with various transport coefficients, including gradient flows, particle–particle interactions, friction matrices, and continuous noise. We achieve this by integrating the collective influence of random and systematic forces acting on the particles within the framework of a Markov chain. We initially validated this method using molecular dynamics simulations of a system subjected to changes in temperatures over time. Subsequently, we conducted further verification using experimental systems reported in the literature and known for their complex nonequilibrium characteristics. The results, including the derived $J(t)$ and other relevant physical parameters, align with the previous observations and reveal detailed dynamical information in nonequilibrium states. This approach represents an advancement in XPCS analysis, addressing the growing demand to extract intricate nonequilibrium dynamics. Further, the methods presented are agnostic to the nature of the material system and can be potentially expanded to hard condensed matter systems.

nonequilibrium dynamics | Langevin dynamics | Markov chain | transport coefficient | X-ray photon correlation spectroscopy

Significance

X-ray photon correlation spectroscopy (XPCS) is increasingly employed to probe dynamics in soft, structured materials, with applications set to grow alongside synchrotron upgrades worldwide. Existing methods often sacrifice crucial details by averaging data, obscuring complex phenomena such as relaxation and avalanches. Our approach, rooted in Langevin dynamics and avoiding averaging, extracts a microscopic $J(t)$ that directly connects to XPCS intensity correlations. This improves our understanding of nonequilibrium dynamics by connecting microscopic insights into macroscopic properties. It opens avenues for optimizing soft materials in various fields, from advanced manufacturing to exploring natural phenomena.

Soft materials, including colloidal suspensions (1, 2), polymers(3, 4), gels (5, 6), and biological materials (7, 8), often exist in nonequilibrium states, a crucial aspect of their practical applications and scientific studies. These nonequilibrium states arise due to external factors, including mechanical forces, temperature fluctuations, or chemical reactions, necessitating an understanding of how these materials respond to such stimuli. Although classical theories such as mean-field theory (9, 10), renormalization group (11, 12), and universality (11, 13) have contributed significantly to our understanding of particle and atomic behavior within complex systems, they fall short when these materials deviate from equilibrium under external influences. Nonequilibrium dynamics introduce intriguing phenomena, including transitions between metastable states (14, 15), dynamical heterogeneity (16, 17), aging (18, 19), yielding (20, 21), avalanches (22, 23), and phase reentrance (24, 25). Real-time measurements serve as a valuable tool to unravel the kinetics and mechanisms governing these transitions, facilitating improved control and predictability (26, 27). Consequently, it becomes imperative to develop robust in situ tools and analysis models that enable us to investigate the dynamic behavior of complex materials (28, 29), validate theoretical constructs (30, 31), and engineer functional materials for a variety of applications within these soft matter systems.

In this pursuit, various in situ techniques, including scattering (32–34), imaging (35–37), spectroscopy (38–41), and force measurements (42, 43), emerge as effective tools for investigating nonequilibrium phenomena. Among these techniques, XPCS, a coherent X-ray scattering method capable of measuring dynamics through the temporal autocorrelation function of intensity fluctuations in space and time, has shone since its introduction in 1991 (44). It offers exceptional spatial and temporal resolution, making it ideal for investigating the unique insight of nonequilibrium dynamics at the nanoscale in diverse soft matter systems. In a typical XPCS experiment (Fig. 1*A*), a series of X-ray scattering intensities (speckles) $I(\vec{q}, t)$ is collected with a 2D detector as a function of time. To extract the dynamics from a nonequilibrium system, a second order two-time

Author affiliations: [a]Materials Science Division and Center for Molecular Engineering, Argonne National Laboratory, Lemont, IL 60439; [b]Pritzker School of Molecular Engineering, University of Chicago, Chicago, IL 60637; and [c]X-Ray Science Division, Advanced Photon Source, Argonne National Laboratory, Lemont, IL 60439

Author contributions: H.H., M.V.T., S.N., and W.C. designed research; H.H. and W.C. performed research; H.H., M.C., Z.J., S.N., and W.C. analyzed data; H.L. conducted molecular dynamics simulations; W.C., M.V.T., J.J.d.P., and S.N. supervised the project; M.V.T. and W.C. conceptualized the research supervised the project; and H.H., H.L., and W.C. wrote the paper.

The authors declare no competing interest.

This article is a PNAS Direct Submission.

[1]To whom correspondence may be addressed. Email: depablo@uchicago.edu, mtirrell@uchicago.edu, sureshn@anl.gov, or wchen@anl.gov.

This article contains supporting information online at https://www.pnas.org/lookup/suppl/doi:10.1073/pnas.2401162121/-/DCSupplemental.

Published July 23, 2024.

intensity autocorrelation function ($c_2(\vec{q}, t_1, t_2)$) is computed according to the following equation (45):

$$c_2(\vec{q}, t_1, t_2) = \frac{\mathbb{E}\left[I(\vec{q}, t_1)I(\vec{q}, t_2)\right]}{\mathbb{E}\left[I(\vec{q}, t_1)\right]\mathbb{E}\left[I(\vec{q}, t_2)\right]}, \quad [1]$$

where notation $\mathbb{E}[...]$ denotes as the ensemble average (*SI Appendix*, section 1).

In a system containing a large number of independent scatters with randomized scattered phases, the scattered fields are generated by Gaussian processes. This condition enables the application of the Siegert relation, and second order two-time intensity autocorrelation function ($c_2(\vec{q}, t_1, t_2)$) is written as follows (46):

$$c_2(\vec{q}, t_1, t_2) = 1 + \beta|c_1(\vec{q}, t_1, t_2)|^2, \quad [2]$$

where $0 \leq \beta \leq 1$ is the coherent contrast depending on the experiment conditions, such as the coherent fraction of X-rays in the incident beam and the size of the pixel in the detector.

The first-order correlation function $c_1(\vec{q}, t_1, t_2)$ is the temporal correlation of the scattered electromagnetic field $E(\vec{q}, t)$:

$$c_1(\vec{q}, t_1, t_2) = \frac{\mathbb{E}\left[E(\vec{q}, t_1)E(\vec{q}, t_2)\right]}{\mathbb{E}\left[E(\vec{q}, t_1)\right]\mathbb{E}\left[E(\vec{q}, t_2)\right]}. \quad [3]$$

A common approach to analyzing equilibrium dynamics $c_2(\vec{q}, t_1, t_2)$ starts with its conversion to a second order one-time intensity autocorrelation function ($g_2(\vec{q}, \tau)$). In equilibrium, $g_2(\vec{q}, \tau)$ is calculated by diagonal averaging of $c_2(\vec{q}, t_1, t_2)$ along the axis of delayed time τ as shown in Fig. 1*B*. However, for nonequilibrium dynamical evolution, diagonal averaging fails, and this conversion thereby involves dividing the absolute time of the experiment into distinct regions, as demonstrated in Fig. 1*C*. These regions are known as TIZs (47). Within these TIZs, it is assumed that the system is in a pseudoequilibrium state. $g_2(\vec{q}, \tau)$ is then calculated by averaging over the delay time $\tau = |t_2 - t_1|$ in either the vertical/horizontal direction or the diagonal direction. Subsequent analysis involves fitting the one-time correlation function with a specific model of the

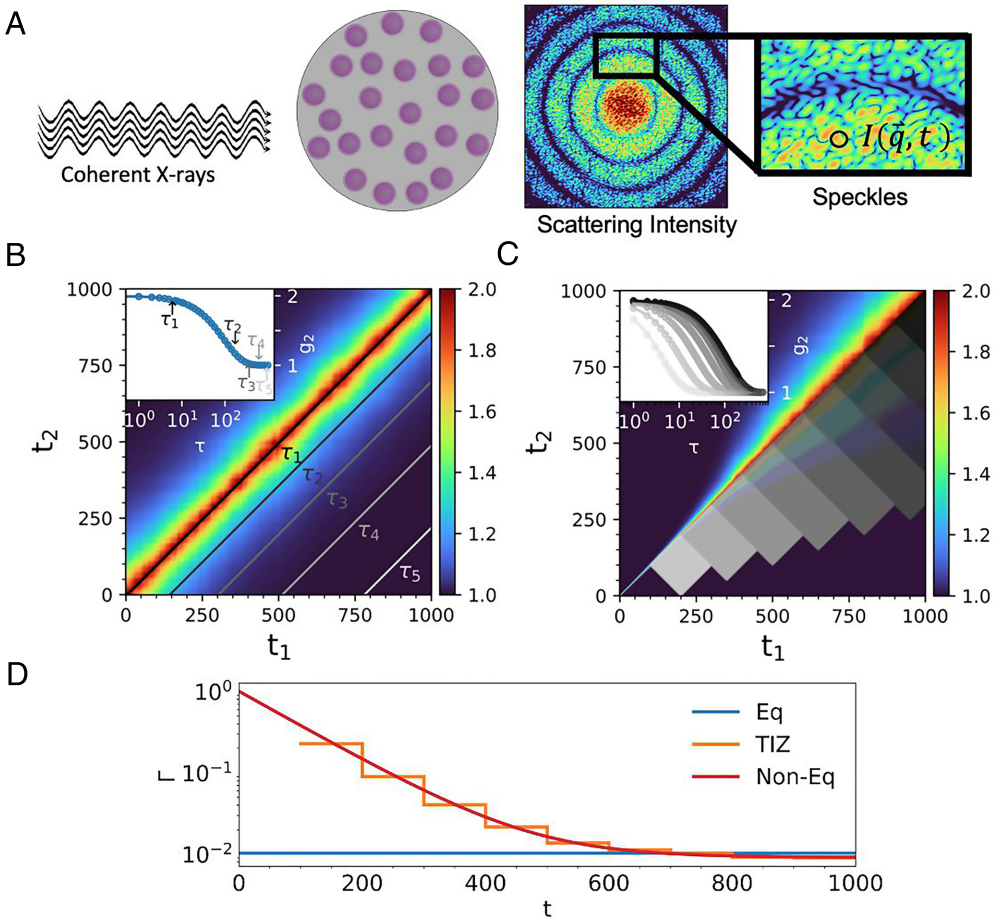

Fig. 1. Illustration of the XPCS experiment procedure and its analysis techniques in both equilibrium and nonequilibrium states. (*A*) In a standard XPCS experiment, coherent X-rays illuminate the samples, generating speckles that reveal the spatial distribution of particles on detectors. Dynamic information about the system is obtained by calculating the temporal correlation function c_2 of these speckles, which is then converted to a one-time correlation function g_2 by averaging. Depending on whether the system is in equilibrium or not, the analysis procedure to convert from c_2 to g_2 varies: In the equilibrium case (*B*), g_2 (*Inset* figure) can be obtained by diagonally averaging c_2 at increasing value of τ (gray line); in contrast, in the nonequilibrium system (*C*), g_2 (*Inset* figure) can only be obtained by averaging c_2 within the predefined TIZs (gray rectangle), where the system is assumed to be pseudoequilibrium for a certain period within the TIZs. The color of g_2 in the *Inset* figure corresponds to the TIZs with lighter colors at an earlier time. (*D*) We introduced a transport coefficient approach to obtain the time-resolved dynamics directly by fitting c_2 without any averaging. As a result of this analysis, Γ represents the characteristic dynamics rate of the system, and its expression depends on the specific system under study. For standard diffusion, it is defined as $\Gamma = q^2D$ in equilibrium (blue line) and $\Gamma(t) = \frac{1}{2}q^2J(t)$ in a nonequilibrium state, where D is the diffusion constant, and $J(t)$ is the transport coefficient, as defined in Eq. **6**. The results obtained from our nonequilibrium analysis approach (red line) offer enhanced detail and higher resolution in the time-resolved dynamics compared to conventional TIZs approaches (orange line).

correlation function tailored to the characteristics of the system under investigation. The choice of an appropriate model depends on the properties and behaviors of the system. For example, a simple exponential function describes the diffusion dynamics with a single relaxation time (48). A Kohlrausch–Williams–Watts (KWW) function has been shown to describe systems that exhibit anomalous diffusion (49), a sinc function for a fluid that undergoes homogeneous shear (50), or a heterodyne scattering function for a system composed of two components with well-separated dynamical time scales (51).

However, XPCS analyses in nonequilibrium systems present significant challenges. Reported studies have treated such systems by approximating the system to be in equilibrium system within TIZs, which is a shortcoming in systems characterized by strongly varying nonequilibrium conditions, such as the combined XPCS and in situ rheology (Rheo-XPCS) experiments conducted under external stimulus (52). Conversion of $c_2(\vec{q}, t_1, t_2)$ into $g_2(\vec{q}, \tau)$ by averaging over τ can potentially distort or overlook intricate time-dependent variations in the data, leading to the loss of crucial information about the dynamics of the system (53). Moreover, current XPCS analyses struggle to decipher complex patterns observed in the two-time correlation function, such as "square," "wings," or "tail-like" features (54–56). Predominant explanations have focused on "backflow" where particles move relative to their neighbors, leading to jammed and disordered arrangements at irregular intervals (47), or abrupt phase transitions of the entire system (54). Such models often overlook the influence of factors such as structural dynamics, particle interactions, and other time-dependent effects that play an important role in shaping the observed patterns. The incomplete consideration of these elements in the current analyses hinders our comprehensive understanding of the underlying dynamics.

Advancing XPCS analysis methodologies in nonequilibrium systems to overcome some of the above limitations is important in deepening our understanding of complex dynamic processes in soft matter. The advancement presented in this work enables the direct extraction of valuable information from $c_2(\vec{q}, t_1, t_2)$ without the need for any temporal averaging. We present a transport coefficient method for characterizing nonequilibrium dynamics in soft matter. Our approach formulates a Langevin dynamics model that considers particle dynamics comprising two constituents: intrinsic random motion and externally driven motion. By assuming a Markovian process without memory for nonequilibrium dynamics, we derive the transition probability $\mathbb{P}(\Delta x, t_1, t_2)$, which connects the probability distribution ($\mathbb{P}$) of position (x) at time t_1 and t_2 within the dynamic process. We then convert this probability to $c_2(\vec{q}, t_1, t_2)$ using a Fourier transform. To validate our model, we initially applied it to a molecular dynamics (MD) simulation system with known physical parameters. This involves comparing the transport coefficient $J(t)$ obtained from the simulation trajectory with the values extracted from the analysis of $c_2(\vec{q}, t_1, t_2)$. Subsequently, we employ this analysis methodology on XPCS results from two sources in the literature that have used existing methodologies: one that involves relaxation of a colloidal system after applied creep (57) and another that involves a gel system subjected to internal stresses (56). Furthermore, we extend our analysis methodology to include complex fluids characterized by even more complex dynamics. In this context, we explore a system involving a suspension of charged colloids in salt solutions. Using a combination of creep measurements and Rheo-XPCS, we delve into the dynamics of deformation and relaxation, allowing us to observe phenomena such as complex patterns in the $c_2(\vec{q}, t_1, t_2)$ and multiple shear bands. Subsequently, we interpret and rationalize these complex rheological phenomena by extracting time-dependent physical quantities using the developed approach. This advancement not only enhances the data accuracy of XPCS analysis (Fig. 1*D*) but also offers significant insight into the dynamical properties of the system that are overlooked by the existing methods.

1. Theoretical Basis

1.1. Langevin Dynamics. Within a given one-dimensional system encompassing nonequilibrium dynamics, the force experienced by an individual particle at any time t, $m\dot{v}(t)$, is expressed through the Langevin equation:

$$\begin{aligned} m\dot{v}(t) &= F_{in}(t) + F_{ex}(t) \\ &= \eta(t) + F_{sys}(x, v, t) + F_{ex}(t), \end{aligned} \quad [4]$$

where $v(t)$ represents the velocity of the particle, and m denotes its mass. F_{in} and F_{ex} are the internal and external forces, respectively. The F_{in} could be further divided into a random force $\eta(t)$ and a systematic force F_{sys}. The term $\eta(t)$ denotes a 'truly random' force or noise, which is independent of the state of motion of the particle. It has an average first moment of zero ($\mathbb{E}[\eta(t)] = 0$) and a second moment average proportional to thermal fluctuations with a strength factor (Γ) as $\mathbb{E}[\eta(t)\eta(t')] = \Gamma\delta(t - t')$. Finally, F_{sys} is a systematic force that depends on the state of motion of the particles.

In a nonequilibrium process displaying Markov chain characteristics, where the likelihood of random motion remains independent of memory, $\mathbb{P}(x, t)$ exhibits Gaussian-like characteristics as:

$$\begin{aligned} \mathbb{P}(x, t) &= \mathcal{N}\left(x; \mu = \mathbb{E}[x(t)], \sigma^2 = \mathbb{V}[x(t)]\right) \\ &= \frac{1}{\sqrt{2\pi\mathbb{V}[x(t)]}} \exp\left(-\frac{(x - \mathbb{E}[x(t)])^2}{2\mathbb{V}[x(t)]}\right). \end{aligned} \quad [5]$$

The center of these probability distributions is determined by the mean position $\mathbb{E}[x(t)]$, while their distribution is contingent upon the variance $\mathbb{V}[x(t)]$ at a given time t.

1.2. Transport Coefficient. Except for a few model systems such as Wiener/standard diffusion (58), Ornstein–Uhlenbeck (59), and Brownian oscillator (60), it remains challenging to obtain an analytical solution of Eq. **4** for the evolution of mean position $\mathbb{E}[x(t)]$ and variance $\mathbb{V}[x(t)]$ of the distribution over time. This is particularly true for systems involving complex particle interactions, hydrodynamic forces, or intricate frictional effects. To quantify the time-resolved dynamic response in any nonequilibrium system, we utilize two time-dependent physical parameters, the mean velocity of the ensemble $\mathbb{E}[v(t)]$ and the dynamical transport coefficient $J(t)$.

In scenarios where the system encounters an external flow field $v_o(t)$, such as applied shear in a rheometer, the main contributor to the mean velocity is this external flow, given by $\mathbb{E}[v(t)] = v_o(t)$. To characterize the internal or random motion of the particles arising from the cumulative influence of various external forces F_{ex}, we employ $J(t)$, which is defined as follows:

$$\begin{aligned} J(t) &= \frac{d}{dt}(\mathbb{V}[x(t)]) = 2\mathrm{Cov}[x(t), v(t)] \\ &= 2\int_0^t \mathrm{Cov}\left[v(t), v(t')\right] \mathrm{d}t'. \end{aligned} \quad [6]$$

This expression explains the physical and mathematical characteristics of $J(t)$ from three aspects:

1. Time derivative of the variance of particles positions as $\frac{d}{dt}(\mathbb{V}[x(t)])$
2. Covariance of $x(t)$ and $v(t)$ as $\mathrm{Cov}[x(t), v(t)]$
3. Integration of velocity correlation function and Green–Kubo formula as $\int_0^t \mathrm{Cov}[v(t), v(t')]\ \mathrm{d}t'$

Traditional transport coefficients, defined and measured in near-equilibrium states, face limitations in far-from-equilibrium situations. The generalized Green–Kubo formula offers an extension for calculating such coefficients in nonequilibrium settings. However, applying this approach requires a more intricate, often system-dependent strategy to accurately describe and predict transport phenomena. While generalized transport coefficients may not fully capture the intricate dynamics at play, it is important to recognize that they can provide valuable insights even away from equilibrium.

1.3. Two-Time Autocorrelation Function. As detailed in the derivation procedure outlined in *SI Appendix*, section 2, $c_1(q, t_1, t_2)$ for nonequilibrium systems with isotropic and uncorrelated noise in every direction, can be described as,

$$c_1(q, t_1, t_2) = c_{1,in}(q, t_1, t_2)c_{1,ex}(q, t_1, t_2). \quad [7]$$

By examining Eq. **7**, we can gain insight into how both the internal and the external dynamics influence $c_1(q, t_1, t_2)$.

The term $c_{1,in}$ contains $J(t)$ to capture the systematic dynamics of the system, as well as the thermal fluctuations it experiences, such as diffusion. These fluctuations exhibit isotropic characteristics, proportional to q^2, due to the presence of uniform noise acting in all directions,

$$c_{1,in}(q, t_1, t_2) = \mathrm{e}^{-\frac{1}{2}q^2 \int_{t_1}^{t_2} J(t)\,\mathrm{d}t}. \quad [8]$$

Conversely, $c_{1,ex}$ is related to the decorrelation resulting from the external field that drives the particles with an average velocity of $\mathbb{E}[v(t)]$ with proportionality to q,

$$c_{1,ex}(q, t_1, t_2) = \mathrm{e}^{iq \int_{t_1}^{t_2} \mathbb{E}[v(t)]\,\mathrm{d}t}. \quad [9]$$

Eq. **7**, along with Eqs. **8** and **9**, describe the two-time correlation function that corresponds to the time-dependent dynamics in a one-dimensional system under the collective influence of all forces, including random force, interaction potential field, drift, and all other possible factors. To disentangle the contribution from each force type, other approaches such as solving for $c_1(q, t_1, t_2)$ or conducting simulations based on the first principles of the specific system become necessary.

Extending Eq. **7** to three-dimensional nonequilibrium systems (*SI Appendix*, section 2.D), such as those with uncorrelated noise in every direction, we define the transport coefficient in every direction as $J_i(t)$, where $i = x, y$, or z. In this context, $c_{1,in}(\vec{q}, t_1, t_2)$ can be expressed as follows:

$$c_{1,in}(\vec{q}, t_1, t_2) = \prod_{i=x,y,z} \mathrm{e}^{-\frac{1}{2}q_i^2 \int_{t_1}^{t_2} J_i(t)\,\mathrm{d}t}, \quad [10]$$

while $c_{1,ex}(\vec{q}, t_1, t_2)$ becomes

$$c_{1,ex}(\vec{q}, t_1, t_2) = \mathrm{e}^{i\vec{q}\cdot \int_{t_1}^{t_2} \mathbb{E}[\vec{v}(t)]\,\mathrm{d}t}. \quad [11]$$

Eqs. **10** and **11** display anisotropic behavior: Maximal effects occur when q aligns with the flow direction, while minimal effects are observed when q is perpendicular to the flow direction.

For purely diffusive systems in which:

1. There is no external drive, such that $\mathbb{E}[\vec{v}(t)] = 0$ or when there is an absence of spatial correlation in particle dynamics resulting in the perfect cancelation of the complex term $c_{1,ex}(\vec{q}, t_1, t_2)$
2. The noise is isotropic in all directions as $J_x = J_y = J_z = \frac{1}{3}J$

the $c_2(\vec{q}, t_1, t_2)$ obtained from an XPCS experiment conducted in a nonequilibrium state can be expressed using the Siegert relation Eq. **2** as follows:

$$c_2(\vec{q}, t_1, t_2) = 1 + \beta \mathrm{e}^{-\frac{1}{3}\left(q_x^2+q_y^2+q_z^2\right)\int_{t_1}^{t_2} J(t)\,\mathrm{d}t}. \quad [12]$$

1.4. External Drive. The introduction of an external drive into the system can significantly impact the decay of the correlation function in the flow direction. When there is a spatial correlation between the particles, their motion can lead to incomplete cancelation of $c_{1,ex}(\vec{q}, t_1, t_2)$. As a result, the complex component, $\left(i\vec{q}\cdot\int_{t_1}^{t_2}\mathbb{E}[\vec{v}(t)]\ \mathrm{d}t\right)$, due to the Doppler shift from the relative motion of the scatters, becomes measurable in the context of $c_2(\vec{q}, t_1, t_2)$ obtained from XPCS experiments. Depending on the flow profiles, various models have been proposed to characterize the system. In the laminar flow that results from steady homogeneous shear between two parallel plates, $c_2(\vec{q}, t_1, t_2)$ is characterized by a homodyne scattering function (50). If the sample comprises two components with relative motion, $c_2(\vec{q}, t_1, t_2)$ is characterized by a heterodyne scattering function (51, 61). In the established works in equilibrium, we further consider nonequilibrium situations when the flow profile is constantly changing over time and the physical parameters that describe the profile are time-dependent functions.

1.4.1. Laminar flow. *SI Appendix*, section 2.E derives $c_2(\vec{q}, t_1, t_2)$ for a laminar flow in nonequilibrium with a shear $\dot{\gamma}(t)$ by considering across numerous flow layers within the gap, resulting expression as follows:

$$c_2(\vec{q}, t_1, t_2) = 1 + \beta\left[\mathrm{e}^{-q^2\int_{t_1}^{t_2} J(t)\,\mathrm{d}t}\right]\times \mathrm{sinc}^2\left[\frac{1}{2}qh\int_{t_1}^{t_2}\dot{\gamma}(t)\cos(\phi(t))\,\mathrm{d}t\right], \quad [13]$$

where h is the gap across the stator and rotor and $\phi(t)$ is the angle between shear/flow direction and $\vec{q}$.

1.4.2. Heterogeneous system. *SI Appendix*, section 2.F describes a complex system combining or mixing two or more components indexed by n, where each component exhibits a time-dependent fraction $x_n(t)$, transport coefficient $J_n(t)$, mean velocity $\mathbb{E}[v_n(t)]$ and angle between the scattering vector and flow direction $\phi_n(t)$, as seen in scenarios such as shear banding in complex fluids (62, 63). The expression for $c_2(\vec{q}, t_1, t_2)$ can be represented as follows:

$$c_2(\vec{q}, t_1, t_2) = 1 + \frac{\beta}{f(t_1, t_2)^2}\sum_{n=1}^{N}\sum_{m=1}^{N}\left[\begin{array}{c} x_n(t_1)x_n(t_2)x_m(t_1)x_m(t_2)\times \\ \mathrm{e}^{-\frac{1}{2}q^2\int_{t_1}^{t_2} J_n(t)+J_m(t)\,\mathrm{d}t}\times \\ \cos\left[q\int_{t_1}^{t_2}\mathbb{E}[v_n(t)]\cos(\phi_n(t)) - \mathbb{E}[v_m(t)]\cos(\phi_m(t))\,\mathrm{d}t\right]\end{array}\right], \quad [14]$$

where $f(t_1, t_2)$ is the normalization factor defined as

$$f(t_1, t_2)^2 = \sum_{n=1}^{N} x_n(t_1)^2 \sum_{n=1}^{N} x_n(t_2)^2. \quad [15]$$

2. Approach Validation

2.1. MD Simulation. To validate the theoretical framework described above, we performed MD simulations involving noninteracting particles (i.e., phantom particles) within a nonequilibrium system created by varying the temperature. As shown in Fig. 2*D*, the temperature was initially maintained at a high value, followed by a linear decrease to a stable lower value. The transport coefficient, $J_{\vec{q}}$, was determined by $c_2(\vec{q}, t_1, t_2)$ using Eq. **12**. To streamline the fitting process, we represented the trend of the transport coefficient using the error function (*SI Appendix*, Eq. **S104**). For a better comparison, in each figure of $c_2(\vec{q}, t_1, t_2)$, the data obtained from experiments and simulation are presented in the *Upper Left*, while the fitting results are displayed in the *Lower Right*. In Fig. 2 *A–C*, $c_2(\vec{q}, t_1, t_2)$ obtained from simulation trajectories with different scattering vectors demonstrates good agreement with the simulated data. According to Eq. **12**, the correlation functions obtained at higher values of $\left(q_x^2 + q_y^2 + q_z^2\right)$ exhibit a faster decay. This trend is evident starting with $\left(q_x = 6, q_y = q_z = 0\right)$ in Fig. 2A, followed by $\left(q_x = q_y = 6, q_z = 0\right)$ in Fig. 2*B*, and subsequently by $\left(q_x = q_y = q_z = 6\right)$ in Fig. 2*C*. Despite these differences, the transport coefficient extracted from $c_2(\vec{q}, t_1, t_2)$ measured with different scattering vectors, namely $J_{q_x=6}(t)$, $J_{q_{x,y}=6}(t)$, and $J_{q_{x,y,z}=6}(t)$, is anticipated to be identical, as they originate from the particle dynamics of the same simulation. This consistency is observed in Fig. 2*D*, where all transport coefficients overlap and follow the same decreasing trend over time. Similar results are also observed for other scattering vectors, as shown in *SI Appendix*, Fig. S5.

In a system without external drive, the transport coefficient can also be obtained directly from simulation trajectories using the time derivative of the mean-squared displacement of particles, denoted as J_{MD} and given by Eq. **6**. This parameter serves as a validation measure for the analysis of $c_2(\vec{q}, t_1, t_2)$. As illustrated in Fig. 2*D*, the transport coefficients obtained by fitting $c_2(\vec{q}, t_1, t_2)$ with different scattering vectors agree with the reference J_{MD}. The slight discrepancy observed for $J_{q_{x,y,z}=6}(t)$ during $t < 100$ can be attributed to two reasons: 1) the absence of valid data to describe the rapid dynamics in the high q regions during the high-temperature period and 2) the selected equation did not accurately capture the actual change in $J(t)$ over time. Despite these imperfections, this result provides evidence that $J(t)$ accurately reflects the actual physical quantity in the system, thus validating the approach of extracting $J(t)$.

2.2. Reported Experiments. After validating the proposed analysis approach through MD simulations, we then confirmed its applicability to the results of previous experiments (56, 57). The relaxation dynamics described in these two respective papers exhibit intriguing dynamic phenomena under nonequilibrium

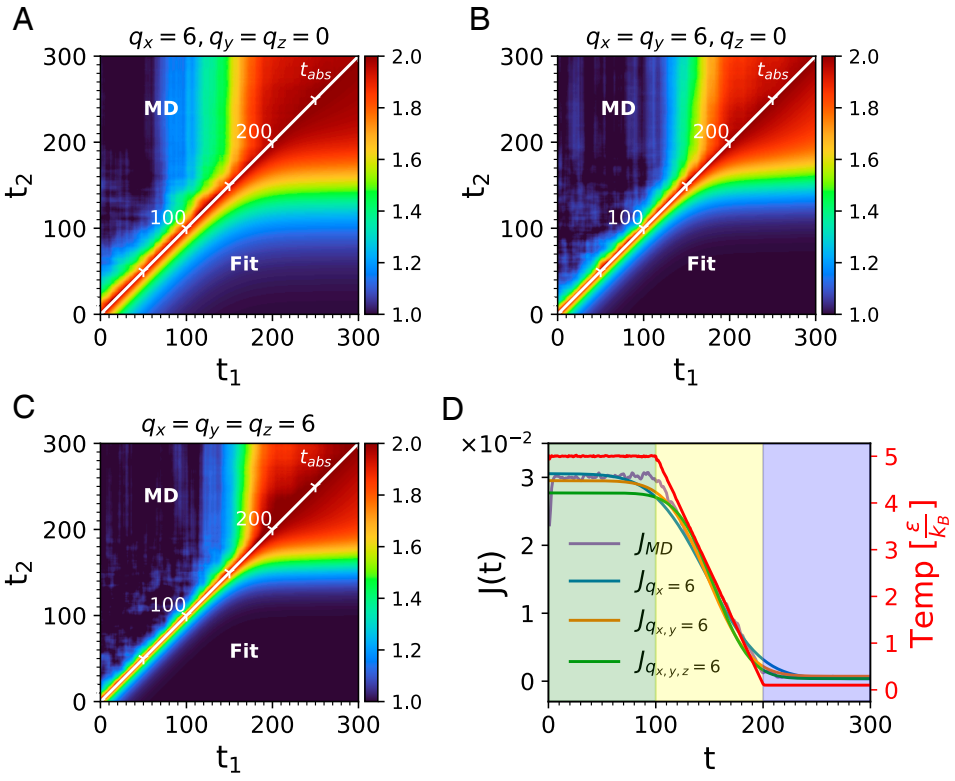

Fig. 2. Simulation of a nonequilibrium system arising from temperature changes and application of transport coefficient analysis to $c_2(\vec{q}, t_1, t_2)$ extracted from different $\vec{q}$ bins. c_2 data are extracted from three bins: (*A*) $(q_x = 6, q_y = q_z = 0)$, (*B*) $(q_x = q_y = 6, q_z = 0)$, and (*C*) $(q_x = q_y = q_z = 6)$. Each c_2 dataset includes fitting results (*Lower Right* corner) and corresponding MD simulation data (*Upper Left* corner) displayed on opposite sides of the diagonal. Panel (*D*) shows the transport coefficient extracted through the analysis in these three bins, $J_{q_x=6}(t)$ (blue line), $J_{q_{x,y}=6}(t)$ (orange line), and $J_{q_{x,y,z}=6}(t)$ (green line), together with the J_{MD} (purple line) calculated directly from the positions of the particles in the simulation box using Eq. **6**. The right-hand red axis illustrates the temperature variation (red line) throughout the simulation.

conditions. The extracted $J(t)$ from our analysis not only corroborates the conclusions presented in the articles but also provides insights into how the particle interactions and drifts resulting from the motion of the particles govern the relaxation dynamics. This is evident from the comparison with the classical model of the Brownian oscillator shown in *SI Appendix*, section 4.B.3.

2.2.1. Overdamped relaxation. The nonequilibrium analysis was applied to investigate relaxation dynamics in a silica particle suspension, as described in recent work by Donley et al. (57). Their data were collected by performing a creep/recovery rheological test with applied stress ranging from 7.5 to 100 Pa for 100 s in a concentrated (42 v%) and disordered suspension of charged silica nanoparticles.

The recovery phase of the creep tests, conducted under stresses of 100 Pa and 10 Pa, was monitored using $c_2(\vec{q}, t_1, t_2)$, which are depicted in Fig. 3*A* and *SI Appendix*, Fig. S6*A*, respectively. To interpret these data, a power-law model was applied, encapsulating the relationship between the transport coefficient ($J(t)$) and time (t), referring to *SI Appendix*, Eq. **S105**. Analysis revealed that $J \sim t^{-1.586}$ accurately represents the transport dynamics during relaxation from the 100 Pa creep/recovery test (Fig. 3*B*), while $J \sim t^{-1.972}$ suitably characterizes the dynamics from the 10 Pa test (*SI Appendix*, Fig. S6*B*). The observed exponential relaxation of $J(t)$ to intrinsic diffusivity of equilibrium (D_o) aligns with the overdamped behavior of a Brownian oscillator (see Table 1 in *Materials and Methods* and *SI Appendix*, Fig. S4 and Eq. **S127**), indicating dominance by systematic drift. This inference is congruent with a system characterized by soft repulsive interactions. The observed power-law decrease of $J(t)$ correlates with the rheometric shear rate via a scaling factor $\frac{k_B T}{\pi r}$, assuming $r = 10$ nm and $T = 298$ K, as specified in the experiments (*SI Appendix*, Fig. S7 at section 5). It is suspected that external shear induces systematic forces by complex potentials, including frictional and interparticle forces, thereby influencing transport dynamics.

Last, the presence of microscopically heterogeneous dynamics is visually substantiated in *SI Appendix*, Fig. S8 of section 6. The distinct "tailing" in *SI Appendix*, Fig. S8*B* indicates the emergence of shear banding, likely due to the abrupt cessation of a thin flow layer near the surface of the rotor in the recovery phase. This observation is in alignment with the previously discussed microscopically heterogeneous dynamics by Donley et al. (57).

2.2.2. Underdamped relaxation. The results from Fig. 3*C* illustrate the application of nonequilibrium analysis to a polymer-particle gel system under mechanical perturbation. This system experienced mechanical perturbation by overloading the cell with the ex situ gelled material, resulting in a compressive strain of approximately 10 % (56). Our study focused on investigating the dynamics and its evolution over time in this gel system. To capture the intricate changes in dynamics, $J(t)$ was determined separately for each experimental time point,

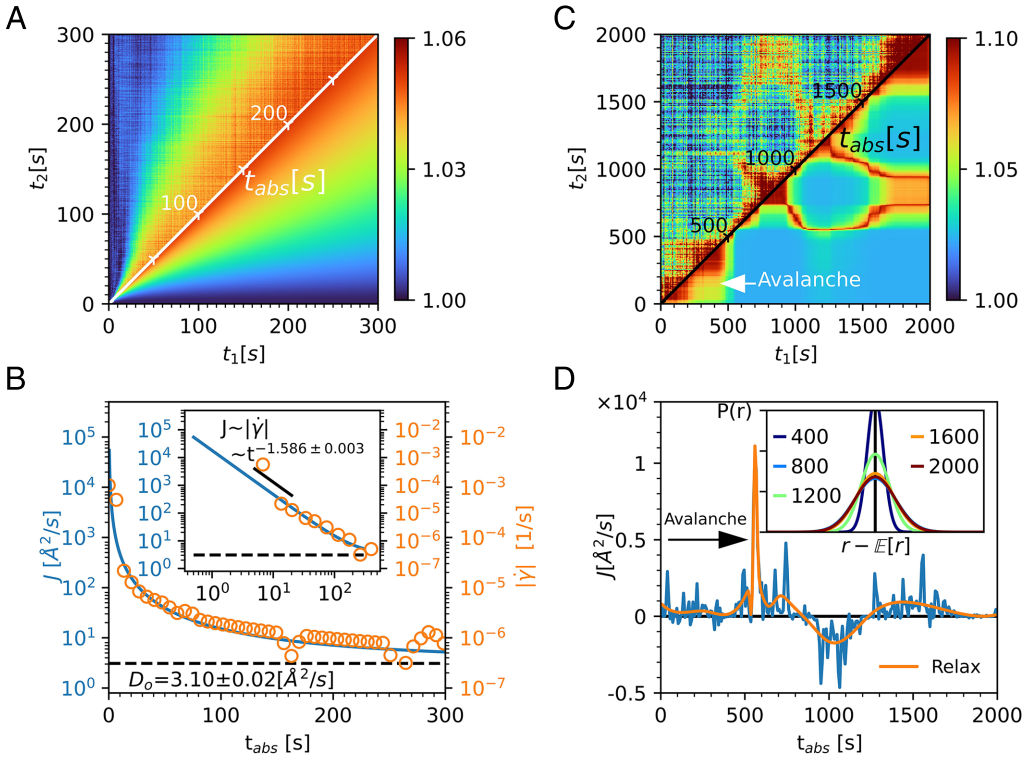

Fig. 3. Verification of the transport coefficient approach using experimental results from previous works. (*A*) Examination of relaxation dynamics in a silica particle suspension reported in Donley et al.'s Rheo-XPCS measurement (57), and (*B*) corresponding results for $J(t)$ (blue line) presented in both linear–log and log–log scales (*Inset*). The orange dots denote $\dot{\gamma}(t)$ simultaneously measured from the rheometer. In the linear–log plot, the black dashed line represents the intrinsic diffusion rate (D_o) of the system under equilibrium conditions, measured at 3.1 Å^2/s. In the log–log plot, the black solid segment depicts the trend of $J(t) \sim |\dot{\gamma}(t)| \sim t^{-1.586 \pm 0.003}$, serving as a visual reference. (*C* and *D*) Application of this nonequilibrium analysis to a gel system subjected to mechanical perturbation, as discussed in the work of Song et al. (56). In (*D*), the blue line depicts the $J(t)$ derived from the nonequilibrium analysis, while the orange line indicates the smoothed $J(t)$, highlighting the relaxation trends. The avalanche dynamics are identified by a white arrow in (*C*), signifying an abrupt decrease followed by a rapid recovery of correlation within $c_2(\vec{q}, t_1, t_2)$. Concurrently, a black arrow in (*D*) marks a notable spike in $J(t)$ at $t = 560$ s, corresponding to the observed avalanche event. Trajectories of $\mathbb{P}(r - \mathbb{E}[r], t)$ are depicted in the *Inset* figure at different time points: $t = 400$ s (blue line), 800 s (cyan line), 1,200 s (green line), 1,600 s (orange line), and 2,000 s (red line), assuming δ-function at $t = 0$. In (*A*) and (*C*), the experimental data are displayed in the *Upper Left* corner, while the fitting results are presented in the *Lower Right* corner.

modeling $c_2(\vec{q}, t_1, t_2)$ by *SI Appendix*, Eq. **S103** as detailed in section 3.A. The observed consistency between the experimental data and the fitting results indicates the successful capture of the dynamic changes as time progresses through nonequilibrium analysis.

The complex shape of $c_2(\vec{q}, t_1, t_2)$ can be attributed to the fluctuation of $J(t)$ in both directions around 0 as the system relaxes from the mechanical perturbation. Experimental $c_2(\vec{q}, t_1, t_2)$ displays a distinctive wings feature, and the correlation function undergoes nonmonotonic changes as the delay time increases. This phenomenon is elucidated by considering the change in the probability density function of particle displacement, denoted as $\mathbb{P}(r-\mathbb{E}[r], t)$. As shown in the *Inset* of Fig. 3*D*, $\mathbb{P}(r-\mathbb{E}[r], t)$ initially broadens ($t = 0 \rightarrow 800$ s) as the system relaxes, but later narrows ($t = 800 \rightarrow 1{,}200$ s) due to the systematic force, reversing its evolution over time. Such behavior in $\mathbb{P}(r-\mathbb{E}[r], t)$ can lead to an initial decrease and subsequent increase in the correlation function without requiring particles to return to their exact positions at earlier times, as observed in previous work (64). The fitting of $J(t)$ reveals that this change in $\mathbb{P}(r-\mathbb{E}[r], t)$ occurs when $J(t)$ becomes negative between 800 and 1,200 s. Notably, $\mathbb{P}(r-\mathbb{E}[r], t)$ at $t = 800$ s and $t = 1{,}600$ s overlaps, indicating that $\mathbb{P}(r-\mathbb{E}[r], t)$ returns to its initial configuration after completing a period of oscillations. The behavior of $J(t)$ is similar to the dissipation dynamics in an underdamped Brownian oscillator when the elastic force dominates the drift force, as shown in Table 1 in *Materials and Methods* and *SI Appendix*, Fig. S3 and Eq. **S126**. However, in this system, F_{sys} is far more complex than a Brownian oscillator potential and drift force, leading to deviations from the classical model, such as $J(t)$ dropping below 0 and its modulation of frequency over time (Fig. 3*D*). However, these oscillations subside, and $J(t)$ approaches 0 at long times, consistent with the predictions of the Brownian oscillator model, aligning with the conclusion that the system returns to equilibrium.

Furthermore, our methodology effectively identifies the occurrence of avalanche dynamics, evidenced at ($t = 560$ s) by a pronounced surge in $J(t)$, as indicated by black arrows in Fig. 3*D*), accompanied by a transient decrease in correlation, swiftly followed by recovery within $c_2(\vec{q}, t_1, t_2)$, as denoted by white arrows in Fig. 3*C*). These avalanche dynamics typically involve the rapid and transient rearrangement of particles, which serves to release the built-up internal stress during the relaxation phase (65), manifesting as a sharp increase in $J(t)$ in XPCS experiments.

In summary, compared to traditional analysis like TIZs approach, our method offers two primary advantages. First, it provides a more granular and quantitatively rich insight into the temporal evolution of system dynamics, as exemplified by the detailed capture of avalanche dynamics at ($t = 560$ s) in Fig. 3*C*, where the enhanced resolution enables the detection and quantification of such intricate phenomena. Second, our technique is particularly adept at uncovering subtle patterns within $c_2(\vec{q}, t_1, t_2)$, such as the tails observed in Fig. 3*A* and the wings patterns in Fig. 3*C*, thereby offering a comprehensive view of the dynamic landscape.

3. Complex Heterogeneity Study

After validating the proposed analysis approach through MD simulations and experimental results from the previous sections, we applied it to a system that exhibits not only significant nonequilibrium characteristics but also heterogeneous dynamic phenomena, such as multiple shear band transitions (66). Investigating the fine dynamics in each shear band of such an opaque colloidal system over time, including its fraction, relative velocity, and rate of intrinsic dynamics, has always been challenging because of limitations in spatiotemporal resolution and penetration depth of instrumental optics, as well as the shortcomings of existing analysis approaches. However, when combined with Rheo-XPCS, our analysis allowed us to explore how $J(t)$ and other physical parameters reflect these complex processes by revealing variations over time that were previously unattainable using conventional analysis methods.

In Fig. 4*A*, we employed nonequilibrium analysis to gain deeper insights into the dynamics of a chosen heterogeneous system. Our focus falls on the shear banding phenomenon observed in Rheo-XPCS experiments, where this approach holds substantial promise for elucidating its underlying mechanisms. This system consists of a combination of spherical silica particles surface-functionalized by L-glutathione (SiO_x-GSH) in a salt suspension containing 60 mM sodium nitrate ($NaNO_3$) and 10 mM magnesium sulfate ($MgSO_4$), with an applied stress of 25 Pa. The Rheo-XPCS measurement of the system displays prominent characteristics of heterodyne scattering as evidenced by the oscillation of the $c_2(\vec{q}, t_1, t_2)$ along the delay time direction. There are two discrete frequencies in oscillations before 15 s and after 40 s, as shown in the zoomed-in section of Fig. 4*A*, indicating the presence of three compositions in the shear banding within these time intervals. The variation in these frequencies over time indicates that the fraction and relative velocity of each composition consistently varies, even diminishes, throughout the creep test. While rheometer measurements yield a standard compliance curve under deformation, the dynamic behaviors provided by Rheo-XPCS, including the velocity (v_{Edge}), fraction (x_n), and transport coefficient (J) of each shear band, once are inaccessible to us due to a lack of an appropriate analysis approach. Therefore, it stands as a compelling example to demonstrate the capabilities of our developed approach to characterize the detailed insights as the change of these physical parameters over time.

In our analysis of nonequilibrium dynamics, we assumed that the system could be represented as comprising a static reference with $v_r = 0$ and $J_r = 0$, along with two components flowing horizontally with mean ensemble velocities of v_1 and v_2, each possessing their respective transport coefficients $J_1(t)$ and $J_2(t)$. We ensured that the angles ϕ_1 and ϕ_2 between the scattering vector $\vec{q}$ and the reference line were equal and denoted as θ, where $\theta = 0$ represents the angle at the flowing direction. These specified conditions allowed us to simplify Eq. **14** and reduce the number of adjustable parameters, as explained in detail in *SI Appendix*, Eqs. **S99**, **S101**, and **S102**. Greater details of the relationship between these physical parameters and time are demonstrated by *SI Appendix*, Eqs. **S106** and **S107** in section 3.D and the fitting results of $c_2(\vec{q}, t_1, t_2)$ in all ϕ directions are shown in *SI Appendix*, section 7.C.

Under the applied stress, the system exhibited a heterogeneous deformation, marked by the formation of three distinct bands: a slow-flowing band, a fast-flowing band, and a static band close to the stator. This formation of three bands can be attributed to the strong attraction between the particles, leading to dense structures in the static and slow-flowing bands and the localization of deformation primarily in the fast-flowing band. As illustrated in Fig. 4*B*, 15 s after initiation of the applied stress ($t = 15$ s), a significant event occurred within the fast-moving band. Most of the particles in this band merged into the slow-moving and

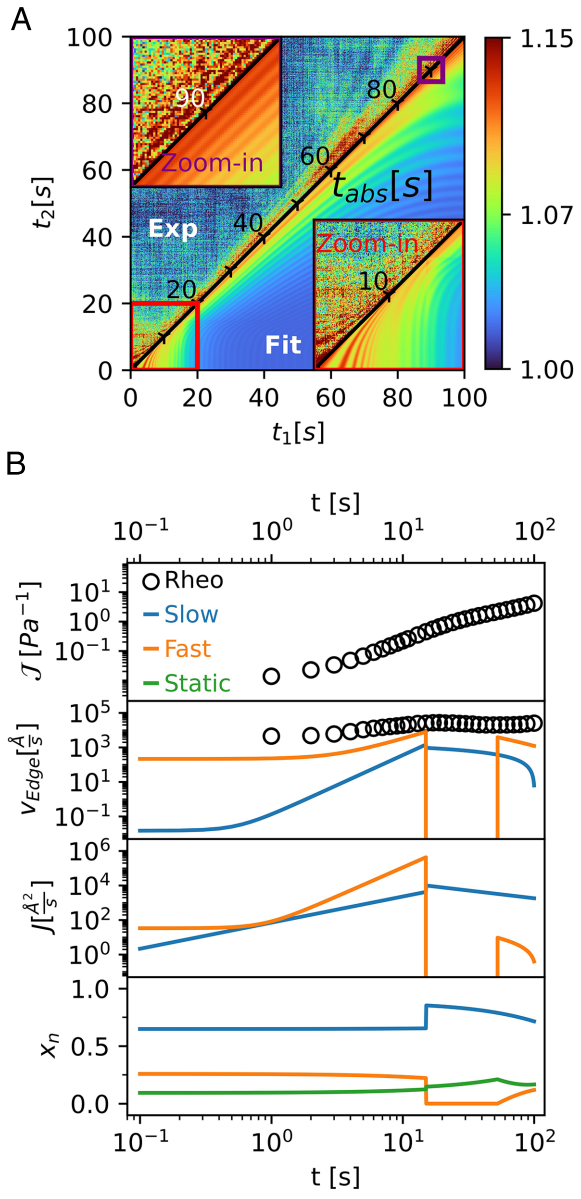

Fig. 4. Application of the transport coefficient approach to a charged particle suspension undergoing shear band transitions during a creep test. (*A*) Observation (*Upper Left* corner) and analysis (*Lower Right* corner) of multiple shear bands in c_2 at flow direction ($\phi = 6.3°$) for a suspension comprising SiO_x-GSH particles in a mixed salt solution (60 mM $NaNO_3$ and 10 mM $MgSO_4$) under constant stress of 25 Pa. The fitting results of $c_2\,(\vec{q}, t_1, t_2)$ in other ϕ direction are shown in *SI Appendix*, section 6. *Insets* in the *Upper* and *Lower* corners illustrate the oscillatory features in c_2 resulting from three shear bands. (*B*) Comparison between rheological measurements and analysis results using the multiple-banding model. The top-to-bottom rows show changes over time in various physical parameters, including compliance ($\mathcal{J}(t)$), the velocity at the outer edge of the rotor (v_{Edge}), transport coefficient $J(t)$, and fraction x_n. These measurements are obtained through direct rheological measurements (black circular markers) and nonequilibrium analysis in XPCS (solid lines), providing insights into the system's dynamics at macro- and microscales, respectively. Within the XPCS measurements, the blue, orange, and green lines specifically track the evolution of the slow, fast, and static bands in the shear banding. To facilitate a more meaningful comparison between the velocity of each band obtained from XPCS and the shear rate $\dot{\gamma}(t)$ measured by the rheometer, $\dot{\gamma}(t)$ is converted to the velocity at the outer edge of the rotor (v_{Edge}) using the equation $v_{Edge}(t) = \dot{\gamma}(t)h$.

static bands, leading to the loss of the fast-moving band as the lubrication layer in the deformation process. Consequently, the entire fast-flowing band transitioned to the slow-flowing state, resulting in a dramatic increase in the fraction of the slow-flowing band. Simultaneously, the increase in shear rate reached a plateau value, and the creep compliance $\mathcal{J}(t)$ increased at a slower rate. After 40 s, the continuously applied stress led to the destruction of the internal structure. Some parts of the static bands started flowing again, with velocities comparable to their prejamming state. Consequently, the fraction of the fast-flowing band gradually increased but velocity decreased over time. Through nonequilibrium analysis, we effectively analyzed the complex dynamics of the multiple shear banding transitions, providing insights into the formation, jamming, and reflow phenomena occurring within the system under applied stress.

4. Conclusion

The proposed transport coefficient, $J(t)$, serves as a comprehensive measure that encapsulates the collective influence of both random and systematic forces on the internal particle dynamics observed in XPCS. This analysis approach for extracting $J(t)$ not only enables us to quantify and understand nonequilibrium dynamics effectively but also allows for a genuine characterization of the system. We have rigorously evaluated its capabilities using both MD simulations and experimental data from previous research. The $J(t)$ obtained through this analysis not only represents the system's underlying physics but also provides nuanced insights beyond the scope of current methodologies.

To further demonstrate its potential, we have applied this method to investigate a complex case that is currently beyond the reach of existing analysis techniques and experiments: a heterogeneous system characterized by shear banding involving three bands, as observed in Rheo-XPCS. We have successfully captured the detailed changes in dynamics within these shear bands, shedding light on how microscale dynamics contribute to the macroscopic rheological response, including shear rate and strain.

In conclusion, our presented method represents a significant advancement in the field of nonequilibrium dynamics analysis and modeling, offering both efficiency and accuracy. Such an advanced approach helps us to better study and understand the intriguing phenomena induced by nonequilibrium dynamics. This understanding can not only be applied to optimizing soft materials in various fields (67, 68), but also holds great potential for exploring natural phenomena (22, 69). Another exciting prospect for future development lies in its potential application to generate extensive datasets, facilitating the training of AI systems to extract nonequilibrium dynamics effectively right after an experiment. This AI tool could prove invaluable in future XPCS beamlines, enabling users to not only optimize experimental conditions before conducting experiments but also provide real-time results and feedback on dynamic systems during XPCS scans. As synchrotron light sources undergo upgrades, offering greater flux and coherence, finer dynamics become accessible in XPCS. In light of these forthcoming advances, our analysis approach holds tremendous promise for immediate application in XPCS studies across a wide range of samples, allowing us to probe subtle nonequilibrium dynamics that were previously inaccessible.

5. Materials and Methods

5.1. Sample Preparation. The charged colloidal systems are created through a chemical process involving the grafting of charged molecules, specifically

Table 1. $J(t)$ from three classical Langevin processes

Langevin process	$J(t)$
Wiener/Standard diffusion	$2D$
Ornstein–Uhlenbeck	$2D\left(1-e^{-\gamma t}\right)^2$
Brownian oscillator: underdamped $\left(\omega_o > \frac{\gamma}{2}\right)$	$2D\frac{\gamma^2}{\omega_s}e^{-\gamma t}\sin^2(\omega_s t)$
Brownian oscillator: overdamped $\left(\omega_o < \frac{\gamma}{2}\right)$	$8D\frac{\gamma^2}{\gamma_s}e^{-\gamma t}\sin^2(\omega_s t)$

L-glutathione (GSH), onto the surfaces of 120 nm spherical silica particles (SiO_x) particles using click chemistry. Once these desired charged particles are obtained, they are suspended in salt solutions (48 v%) comprising 60 mM $NaNO_3$ + 10 mM $MgSO_4$. The suspensions are then subjected to an ultrasonic treatment. The volume fraction of the system is intentionally designed to strike a delicate balance–it is sufficiently high to encourage the development of an internal structure, yet low enough to prevent occurrences of glass transition and crystallization.

5.2. Rheo-XPCS. The XPCS experiment takes place at 8ID-I at Advanced Photon Source in Argonne National Laboratory, with a sample-to-detector distance of 8 m, X-ray energy set at 7.35 keV, and data acquisition at a rate of 10 Hz. Simultaneously, a Rheo-XPCS experiment is conducted by performing a creep test. This approach allows for the measurement of both deformation under constant applied stress and the subsequent recovery after stress removal, enabling a comprehensive study of the system's yielding behaviors. In the context of charged colloids that exist under complex ionic conditions, this setup anticipates a range of intricate rheological phenomena, including delayed yielding, resolidification, and shear banding. In the Rheo-XPCS experiment, the creep test is performed on SiO_x-GSH in a solution consisting of 60 mM $NaNO_3$ + 10 mM $MgSO_4$. In particular, the deformation behavior of SiO_x-GSH in this specific ionic environment exhibits heterodyne scattering signals characterized by multiple shear bands, as illustrated in Fig. 4*A*. Given the complexity of this phenomenon, more in-depth analysis and interpretation are warranted, using the nonequilibrium analysis of XPCS as described in this study.

5.3. MD Simulation. The solvent is implicitly modeled by the Langevin thermostat, and the equation of motion of the i-th particle is

$$\dot{\vec{v}}_i = -\gamma\vec{v}_i + \frac{\vec{\eta}_i(t)}{m}, \qquad [16]$$

where the mass, m, is set to unity for all particles, $\vec{v}_i(t)$ is the velocity of the i-th particle. The stochastic force acting on the i-th particle, $\vec{\eta}_i(t)$, satisfies the following conditions,

$$\begin{aligned}\mathbb{E}\left[\vec{\eta}_i(t)\right] &= 0\\ \mathbb{E}\left[\vec{\eta}_i(t)\cdot\vec{\eta}_j(t')\right] &= 6k_BT\gamma\delta_{ij}\delta(t-t').\end{aligned} \qquad [17]$$

The friction coefficient, γ, is set to $\gamma = 100\frac{m}{\tau}$, where $\tau = \sigma\left(\frac{m}{\epsilon}\right)^{\frac{1}{2}}$ is the reduced time, σ and ϵ are reduced length and energy, respectively. The velocity-Verlet algorithm is used to integrate the equation of motion, with an integration time step $\Delta t = 0.001\tau$. The simulation consists of three stages with different temperatures:

1. The temperature was kept constant at $T = 5\frac{\epsilon}{k_B}$.
2. The temperature linearly decreased with time from $T = 5\frac{\epsilon}{k_B}$ to $T = 0.1\frac{\epsilon}{k_B}$.
3. The temperature remained constant at $T = 0.1\frac{\epsilon}{k_B}$.

Each stage lasts for 1τ (i.e., 1,000 simulation steps). All simulations were performed using the large-scale atomic/molecular massively parallel simulator (LAMMPS) (70) under the periodic boundary condition.

5.4. $J(t)$ from three classical Langevin processes. Table 1 presents the formulations for the $J(t)$s derived from three classical Langevin dynamics. In this context, D represents the classical diffusion constant in the equilibrium state. The symbol γ denotes the drift velocity, indicative of the average directional motion, while ω_0 represents the angular frequency associated with the harmonic oscillator's oscillations. The terms γ_S and ω_S are dimensionless parameters corresponding to scaled versions of γ and ω_0.

In the case of an underdamped Brownian oscillator, where the influence of the elastic force surpasses that of the drift force $\left(\omega_0 > \frac{\gamma}{2}\right)$, $J(t)$ oscillates over time due to the $\sin^2(\omega_S t)$ component. Conversely, in an overdamped oscillator scenario $\left(\omega_0 < \frac{\gamma}{2}\right)$ characterized by the predominance of the drift force, the oscillatory behavior of $J(t)$, driven by $\sinh^2\left(\frac{1}{2}\gamma_S t\right)$, dissipates more rapidly. Further elaboration on this topic is provided in *SI Appendix*, section 4.

Data, Materials, and Software Availability. All study data are included in the article and/or *SI Appendix*.

ACKNOWLEDGMENTS. We extend our gratitude to Professor Mark Sutton for his inspiring discussions and his thorough examination of equation derivations. Work in the Materials Science Division and Center for Molecular Engineering of Argonne National Laboratory was supported by the U.S. Department of Energy, Office of Science, Office of Basic Energy Sciences, Materials Science and Engineering Division. Miaoqi Chu, Zhang Jiang, and Suresh Narayanan, who contributed to the XPCS data analysis, received partial support from the Laboratory Directed Research and Development program at Argonne National Laboratory. This research used resources of the Advanced Photon Source and the Center for Nanoscale Materials, two U.S. Department of Energy (DOE) Office of Science User Facilities operated for the DOE Office of Science by Argonne National Laboratory under Contract No. DE-AC02-06CH11357. In addition, we gratefully acknowledge the computing resources provided on Bebop, a high-performance computing cluster operated by the Laboratory Computing Resource Center at Argonne National Laboratory. This work was completed in part with resources provided by the University of Chicago's Research Computing Center.

1. E. Senses *et al.*, Small particle driven chain disentanglements in polymer nanocomposites. *Phys. Rev. Lett.* **118**, 147801 (2017).
2. H. Guo *et al.*, Entanglement-controlled subdiffusion of nanoparticles within concentrated polymer solutions. *Phys. Rev. Lett.* **109**, 055901 (2012).
3. T. Rosén *et al.*, Exploring nanofibrous networks with X-ray photon correlation spectroscopy through a digital twin. *Phys. Rev. E* **108**, 014607 (2023).
4. R. A. Narayanan *et al.*, Dynamics and internal stress at the nanoscale related to unique thermomechanical behavior in polymer nanocomposites. *Phys. Rev. Lett.* **97**, 075505 (2006).
5. E. Geissler, K. Kosik, A. Fluerasu, A. Moussaïd, K. László, "X-ray photon correlation spectroscopy of dynamics in thermosensitive gels" in *Macromolecular Symposia* (Wiley Online Library, 2007), vol. 256, pp. 73–79.
6. A. Jain *et al.*, Three-step colloidal gelation revealed by time-resolved X-ray photon correlation spectroscopy. *J. Chem. Phys.* **157**, 184901 (2022).
7. L. B. Lurio, G. M. Thurston, Q. Zhang, S. Narayanan, E. M. Dufresne, Use of continuous sample translation to reduce radiation damage for XPCS studies of protein diffusion. *J. Synchrot. Rad.* **28**, 490–498 (2021).
8. J. Möller, M. Sprung, A. Madsen, C. Gutt, X-ray photon correlation spectroscopy of protein dynamics at nearly diffraction-limited storage rings. *IUCrJ* **6**, 794–803 (2019).
9. J. W. Negele, The mean-field theory of nuclear structure and dynamics. *Rev. Mod. Phys.* **54**, 913 (1982).
10. H. Flyvbjerg, K. Sneppen, P. Bak, Mean field theory for a simple model of evolution. *Phys. Rev. Lett.* **71**, 4087 (1993).
11. R. W. Batterman, Why equilibrium statistical mechanics works: Universality and the renormalization group. *Philos. Sci.* **65**, 183–208 (1998).
12. G. Jona-Lasinio, Renormalization group and probability theory. *Phys. Rep.* **352**, 439–458 (2001).
13. L. P. Kadanoff, Scaling and universality in statistical physics. *Physica A* **163**, 1–14 (1990).
14. P. N. Pusey, W. Van Megen, Phase behaviour of concentrated suspensions of nearly hard colloidal spheres. *Nature* **320**, 340–342 (1986).
15. M. Cates, S. Fielding, D. Marenduzzo, E. Orlandini, J. Yeomans, Shearing active gels close to the isotropic-nematic transition. *Phys. Rev. Lett.* **101**, 068102 (2008).
16. S. Lerouge, M. Argentina, J. P. Decruppe, Interface instability in shear-banding flow. *Phys. Rev. Lett.* **96**, 088301 (2006).
17. J. B. Salmon, A. Colin, S. Manneville, F. Molino, Velocity profiles in shear-banding wormlike micelles. *Phys. Rev. Lett.* **90**, 228303 (2003).
18. M. Cloitre, R. Borrega, L. Leibler, Rheological aging and rejuvenation in microgel pastes. *Phys. Rev. Lett.* **85**, 4819 (2000).

19. M. B. Gordon, C. J. Kloxin, N. J. Wagner, The rheology and microstructure of an aging thermoreversible colloidal gel. *J. Rheol.* **61**, 23–34 (2017).
20. P. Sollich, F. Lequeux, P. Hébraud, M. E. Cates, Rheology of soft glassy materials. *Phys. Rev. Lett.* **78**, 2020 (1997).
21. P. Jop, V. Mansard, P. Chaudhuri, L. Bocquet, A. Colin, Microscale rheology of a soft glassy material close to yielding. *Phys. Rev. Lett.* **108**, 148301 (2012).
22. K. A. Dahmen, Y. Ben-Zion, J. T. Uhl, Micromechanical model for deformation in solids with universal predictions for stress–strain curves and slip avalanches. *Phys. Rev. Lett.* **102**, 175501 (2009).
23. K. A. Dahmen, Y. Ben-Zion, J. T. Uhl, A simple analytic theory for the statistics of avalanches in sheared granular materials. *Nat. Phys.* **7**, 554–557 (2011).
24. B. J. Landrum, W. B. Russel, R. N. Zia, Delayed yield in colloidal gels: Creep, flow, and re-entrant solid regimes. *J. Rheol.* **60**, 783–807 (2016).
25. E. Moghimi, A. B. Schofield, G. Petekidis, Yielding and resolidification of colloidal gels under constant stress. *J. Phys.: Condens. Matter* **33**, 284002 (2021).
26. J. Wang, Landscape and flux theory of non-equilibrium dynamical systems with application to biology. *Adv. Phys.* **64**, 1–137 (2015).
27. A. Das, D. T. Limmer, Nonequilibrium design strategies for functional colloidal assemblies. *Proc. Natl. Acad. Sci. U.S.A.* **120**, e217242120 (2023).
28. M. T. Valentine *et al*., Investigating the microenvironments of inhomogeneous soft materials with multiple particle tracking. *Phys. Rev. E* **64**, 061506 (2001).
29. M. Nabizadeh *et al*., Network physics of attractive colloidal gels: Resilience, rigidity, and phase diagram. *Proc. Natl. Acad. Sci. U.S.A.* **121**, e2316394121 (2024).
30. G. P. Morriss, D. J. Evans, Isothermal response theory. *Mol. Phys.* **54**, 629–636 (1985).
31. G. P. Morriss, D. J. Evans, Application of transient correlation functions to shear flow far from equilibrium. *Phys. Rev. A* **35**, 792 (1987).
32. Z. Wang *et al*., Fingerprinting molecular relaxation in deformed polymers. *Phys. Rev. X* **7**, 031003 (2017).
33. S. Pandey *et al*., Time-resolved serial femtosecond crystallography at the European XFEL. *Nat. Methods* **17**, 73–78 (2020).
34. T. Rosén *et al*., Shear-free mixing to achieve accurate temporospatial nanoscale kinetics through scanning-SAXS: Ion-induced phase transition of dispersed cellulose nanocrystals. *Lab Chip* **21**, 1084–1095 (2021).
35. D. F. Arola, G. A. Barrall, R. L. Powell, K. L. McCarthy, M. J. McCarthy, Use of nuclear magnetic resonance imaging as a viscometer for process monitoring. *Chem. Eng. Sci.* **52**, 2049–2057 (1997).
36. P. J. Lu, P. A. Sims, H. Oki, J. B. Macarthur, D. A. Weitz, Target-locking acquisition with real-time confocal (TARC) microscopy. *Opt. Exp.* **15**, 8702–8712 (2007).
37. A. Barty *et al*., Ultrafast single-shot diffraction imaging of nanoscale dynamics. *Nat. Photon.* **2**, 415–419 (2008).
38. A. Arcovito *et al*., X-ray structure analysis of a metalloprotein with enhanced active-site resolution using in situ X-ray absorption near edge structure spectroscopy. *Proc. Natl. Acad. Sci. U.S.A.* **104**, 6211–6216 (2007).
39. M. Maiuri, M. Garavelli, G. Cerullo, Ultrafast spectroscopy: State of the art and open challenges. *J. Am. Chem. Soc.* **142**, 3–15 (2019).
40. Y. H. Wang *et al*., In situ Raman spectroscopy reveals the structure and dissociation of interfacial water. *Nature* **600**, 81–85 (2021).
41. J. S. Gardner, G. Ehlers, A. Faraone, V. García Sakai, High-resolution neutron spectroscopy using backscattering and neutron spin-echo spectrometers in soft and hard condensed matter. *Nat. Rev. Phys.* **2**, 103–116 (2020).
42. D. Garcia-Sanchez, K. Y. Fong, H. Bhaskaran, S. Lamoreaux, H. X. Tang, Casimir force and in situ surface potential measurements on nanomembranes. *Phys. Rev. Lett.* **109**, 027202 (2012).
43. C. Liu, S. Ye, In situ atomic force microscopy (AFM) study of oxygen reduction reaction on a gold electrode surface in a dimethyl sulfoxide (DMSO)-based electrolyte solution. *J. Phys. Chem. C* **120**, 25246–25255 (2016).
44. M. Sutton *et al*., Observation of speckle by diffraction with coherent X-rays. *Nature* **352**, 608–610 (1991).
45. G. Fuller, J. Rallison, R. Schmidt, L. Leal, The measurement of velocity gradients in laminar flow by homodyne light-scattering spectroscopy. *J. Fluid Mech.* **100**, 555–575 (1980).
46. B. Chu, *Laser Light Scattering: Basic Principles and Practice* (Courier Corporation, 2007).
47. Y. Chen, S. A. Rogers, S. Narayanan, J. L. Harden, R. L. Leheny, Microscopic dynamics of stress relaxation in a nanocolloidal soft glass. *Phys. Rev. Mater.* **4**, 035602 (2020).
48. S. Dierker, R. Pindak, R. Fleming, I. Robinson, L. Berman, X-ray photon correlation spectroscopy study of Brownian motion of gold colloids in glycerol. *Phys. Rev. Lett.* **75**, 449 (1995).
49. R. Bandyopadhyay *et al*., Evolution of particle-scale dynamics in an aging clay suspension. *Phys. Rev. Lett.* **93**, 228302 (2004).
50. W. R. Burghardt, M. Sikorski, A. R. Sandy, S. Narayanan, X-ray photon correlation spectroscopy during homogenous shear flow. *Phys. Rev. E* **85**, 021402 (2012).
51. C. Gutt *et al*., Observation of heterodyne mixing in surface X-ray photon correlation spectroscopy experiments. *Phys. Rev. Lett.* **91**, 076104 (2003).
52. R. L. Leheny, M. C. Rogers, K. Chen, S. Narayanan, J. L. Harden, Rheo-XPCS. *Curr. Opin. Colloid Interface Sci.* **20**, 261–271 (2015).
53. O. Bikondoa, On the use of two-time correlation functions for X-ray photon correlation spectroscopy data analysis. *J. Appl. Crystall.* **50**, 357–368 (2017).
54. A. Ragulskaya *et al*., Reverse-engineering method for XPCS studies of non-equilibrium dynamics. *IUCrJ* **9**, 439–448 (2022).
55. A. Ragulskaya, "Dynamics of liquid-liquid phase separation in protein solutions probed by coherent X-ray scattering," PhD thesis, Universität Tübingen (2023).
56. J. Song *et al*., Microscopic dynamics underlying the stress relaxation of arrested soft materials. *Proc. Natl. Acad. Sci. U.S.A.* **119**, e2201566119 (2022).
57. G. J. Donley *et al*., Investigation of the yielding transition in concentrated colloidal systems via rheo-XPCS. *Proc. Natl. Acad. Sci. U.S.A.* **120**, e2215517120 (2023).
58. A. Einstein *et al*., On the motion of small particles suspended in liquids at rest required by the molecular-kinetic theory of heat. *Ann. Phys.* **17**, 208 (1905).
59. G. E. Uhlenbeck, L. S. Ornstein, On the theory of the Brownian motion. *Phys. Rev.* **36**, 823 (1930).
60. S. Chandrasekhar, Stochastic problems in physics and astronomy. *Rev. Mod. Phys.* **15**, 1 (1943).
61. F. Livet *et al*., X-ray intensity fluctuation spectroscopy by heterodyne detection. *J. Synchrot. Rad.* **13**, 453–458 (2006).
62. S. A. Rogers, D. Vlassopoulos, P. Callaghan, Aging, yielding, and shear banding in soft colloidal glasses. *Phys. Rev. Lett.* **100**, 128304 (2008).
63. V. Chikkadi, D. Miedema, M. Dang, B. Nienhuis, P. Schall, Shear banding of colloidal glasses: Observation of a dynamic first-order transition. *Phys. Rev. Lett.* **113**, 208301 (2014).
64. M. C. Rogers *et al*., Microscopic signatures of yielding in concentrated nanoemulsions under large-amplitude oscillatory shear. *Phys. Rev. Mater.* **2**, 095601 (2018).
65. T. Niiyama, M. Wakeda, T. Shimokawa, S. Ogata, Structural relaxation affecting shear-transformation avalanches in metallic glasses. *Phys. Rev. E* **100**, 043002 (2019).
66. E. Miller, J. P. Rothstein, Transient evolution of shear-banding wormlike micellar solutions. *J. Non-Newtonian Fluid Mech.* **143**, 22–37 (2007).
67. A. M'barki, L. Bocquet, A. Stevenson, Linking rheology and printability for dense and strong ceramics by direct ink writing. *Sci. Rep.* **7**, 6017 (2017).
68. Z. Li *et al*., Fresh and hardened properties of extrusion-based 3D-printed cementitious materials: A review. *Sustainability* **12**, 5628 (2020).
69. I. Loftus, "Chapter 4: Mechanisms of Plaque Rupture." in *Mechanisms of Vascular Disease: A Reference Book for Vascular Specialists,* R. Fitridge, M. Thompson, Eds. (University of Adelaide Press, Adelaide, SA, Australia, 2011).
70. S. Plimpton, Fast parallel algorithms for short-range molecular dynamics. *J. Comput. Phys.* **117**, 1–19 (1995).